Check for updates

Decrypting the hydrogen evolution in alkaline water with novel magnetoactive cobalt(II) complex-driven cobalt oxide electrocatalysts†

Subhajit Saha, [ID] [a] Nilankar Diyali, [ID] [a] Sangharaj Diyali,[a] Subhra Jyoti Panda,[b] Mainak Das,[c] Sobhna Acharya,[d] Prafullya Kumar Mudi,[e] Monika Singh, [ID] [d] Partha Pratim Ray,[c] Chandra Shekhar Purohit [ID] [b] and Bhaskar Biswas [ID] *[a]

Under the gravity of future socio-economic development, the viability of water electrolysis still hinges on the accessibility of stable earth-abundant electrocatalysts and net energy efficiency. This work emphasizes the design and synthesis of two newly developed cobalt(II) complexes, $[Co(HL)_2(NCS)_2]$ (**Co^mono**) and $[Co_2(L)_3(CH_3OH)]ClO_4$ (**Co^di**), with a (N,O)-donor ligand, H**L** (2-methoxy-6-(((2-methoxyphenyl)imino) methyl)phenol). The study delves into understanding their structural, morphological, magnetic, and charge transport characteristics. Moreover, the study explores the potential of these complexes in catalyzing hydrogen production through heterogeneous electrocatalysis. The X-ray crystal structure of **Co^mono** reveals the octahedral geometry of the Co(II) ion, adopting two HL units and two NCS⁻ units. The **Co^di** complex exhibits a doubly-phenoxo-O-bridged ($\mu_{1,1}$) dinuclear complex, forming a typical octahedral geometry for both the Co(II) centres in coupling with three units of **L**⁻. Temperature-dependent magnetic susceptibility measurements showed that all of the Co(II) ion in **Co^mono** shows a typical paramagnetic behaviour for high spin octahedral Co(II) ions while the Co(II) centres in **Co^di** are coupled with doubly-phenoxo-bridges bearing weak ferromagnetic characteristics at low temperature. Electron transport properties of the Co(II) complex-mediated Schottky device address the superior carrier mobility (μ) for **Co^di** (9.21×10^{-5}) over **Co^mono** (2.02×10^{-5} m² v⁻¹ s⁻¹) with respective transit times of 1.70×10^{-9} and 7.77×10^{-9} s. Additionally, electron impedance spectral analysis supports the lower electrical transport resistance of **Co^di** relative to **Co^mono**. The heterogeneous electrocatalytic HER activity of **Co^di** and **Co^mono** in 0.1 M KOH shows excellent electrocatalytic efficiency in terms of the various electrochemical parameters. Constant potential electrolysis, multi-cycle CVs, and post-HER analysis reveal the pre-catalytic nature of the complexes, which in turn delivers Co_3O_4 nanoparticles as the active catalysts for efficient hydrogen evolution.

ᵃDepartment of Chemistry, University of North Bengal, Darjeeling-734013, India.
E-mail: bhaskarbiswas@nbu.ac.in,, icbbiswas@gmail.com
ᵇDepartment of Chemical Sciences, National Institute of Science Education and Research, Bhubaneswar 752050, India
ᶜDepartment of Physics, Jadavpur University, Kolkata-700032, India
ᵈEnergy and Environment Unit, Institute of Nano Science and Technology, Mohali 140306, India
ᵉDepartment of Chemistry, University of Burdwan, Burdwan 713104, India

Introduction

Hydrogen has been hailed as a green fuel for the future and has marked its place as a clean and renewable energy and net-zero emission source for environmental sustainability.[1] It is the most abundant element in the universe with a huge calorific value. Hydrogen energy is different from "movement energy" such as electricity, water energy, and wind energy and is treated as a "carrier energy".[2,3] Therefore, it offers a foundation for a new way of energy storage through water electrolysis and might become a giant platform for the hydrogen economy. Under the gravity of the energy crisis and alarming ecological ailment, sustainable hydrogen production has attracted intensive attention from modern researchers. In the last decade, incredible breakthroughs have been achieved in electrocatalytic H_2 production in acidic and alkaline electrolytes, with striking results in this domain.[4,5] However, the development of benchmark electrocatalysts featuring low overpotential, higher stability, and longevity under electrochemical conditions, cost-effectiveness, and excellent turnover frequency

for the proton reduction reaction still remains a formidable challenge, aiming to commercialize green energy across the globe.[6,7]

Rationally designed coordination compounds have emerged as exciting molecular catalysts for pursuing excellent functional activities, particularly the active sites of metalloenzymes.[8–11] Notably, coordination compounds offer vast possibilities for metal–ligand coordination, synergism, and facile control of the coordination environment, enabling them to be a promising platform for electrocatalytic applications.[7] Ligands play a substantial role in the decoration of molecular complexes as electrocatalysts.[12]

Amongst the availability of different ligands, Schiff bases stand out as an important class of ligands for the judicious design of metal complexes owing to their preparative accessibility, facile tuning of donor sites, and introduction of flexibility in the ligand backbone.[13–15]

Additionally, the preferential choice of metal ions for the preparation of metal complexes is as crucial as the ligands. So far, many researchers have designed and developed molecular electrocatalysts based on earth-abundant 3d-metal ions in coupling with tailor-made ligands with remarkable overpotential and turnover numbers.[7] However, cobalt-based molecular electrocatalysts have marked their distinctive footprints in the electrocatalytic hydrogen evolution activities due to their abundant reserves, low cost, and small energy barrier for H adsorption.[16]

In general, cobalt complexes have been evaluated as electrocatalysts for hydrogen evolution reaction (HER) in the non-aqueous medium using an acid source as well as in buffer media.[17] Recently, Padhi and researchers developed two dinuclear cobalt(II) complexes bearing benzimidazole-derived redox-active ligands for electrocatalytic proton reduction in DMF–water (V/V, 95/5) mixture using acetic acid and elucidated the role of electronegative substituents in monitoring the catalytic activity through electron-coupled-proton transfer mechanistic routes.[18] However, cobalt-based molecular electrocatalysts are prone to hydrolysis in the aqueous-alkaline medium. Typically, the molecular complexes undergo significant structural transformations under operational conditions, and therefore, the stability issue limits the use of molecular catalysts in alkaline HER.[19] On the contrary, heterogeneous electrocatalytic HER-mediated by molecular complexes in alkaline conditions has marked several advantages in terms of stability, easy separation, recyclability, and high tolerance factor, where supports like carbon nanotube (CNT),[20] graphene oxide (GO),[21] and nickel form (NF)[22] play vital roles for the deliberation of highly efficient electrocatalysts. Recently, M. Natali and researchers reported the excellent electrocatalytic activities of cobalt(II)–polypyridine complexes immobilized on single-walled carbon nanohorns (SWCNHs) with an overpotential of 0.52 V in 1 M phosphate buffer (pH = 7.4).[23] Further, K. Kumar and team developed a heterogeneous electrocatalyst consisting of cobal-toxime complexes anchored on activated carbon cloth (CC) with 334 mV@10 mA cm^{-2} in an alkaline medium.[24] Furthermore, R. G. Doria and group developed a multi-walled

carbon nanotube-supported cobalt–dithiolene complex-mediated heterogeneous catalyst for hydrogen evolution studies with a remarkable TON = 50 980 in pH 7 medium.[25] S. Vasudevan and the group reported two mononuclear cobalt(II) complexes, $[Co(OH_2)_2(PMBP)_2]$, and $[Co(OH_2)_2(PMTP)_2]$, which exhibited overpotentials of −0.91 and −0.77 V vs. RHE@10 mA cm^{-2}, respectively, in 1 M KOH solution.[26]

Nevertheless, effectual compositional and structural modification to innovate heterogeneous electrochemical characteristics in the electrocatalysts hold great promise, delineating the profound activity of the catalysts.[27] The excellent catalytic performance of HER can be accredited to the upsurge of active sites, surface/interface regulation, synergistic effects, modulation in electronic structure, and the charge transfer process.[28–30]

In addition, the electron transport and ferromagnetic properties of a material may greatly augment the electrocatalytic activity, triggering a new avenue in the electrocatalyst design.[31] Particularly, materials with large unpaired spins and a low resistance at the electrodes greatly influence the course of electrocatalytic HER.[30,32] Wang and researchers demonstrated that ferromagnetic particles can afford efficient electron transfer from the glassy carbon electrode to active sites under an external vertical magnetic field, leading to an elevation in the HER performance.[33,34] Therefore, determining an electrocatalyst's electron transport and magnetic properties is crucial for labelling its electrocatalytic efficiency.

In this present endeavour, we have prepared an N,O-type Schiff base ligand and synthesized two cobalt(II) complexes, **Co^{mono}** and **Co^{di}**. The compounds were structurally and morphologically characterized with spectroscopic and analytical techniques as well as X-ray crystallography. The electron transport and temperature-dependent magnetic properties were also revealed to assess the electrocatalytic prospects of the complexes. The electrocatalytic fate of the synthetic cobalt(II) catalysts in heterogeneous alkaline HER was comprehensively studied. Constant potential electrolysis, multi-cycle CVs, and post-HER analysis suggest the *in situ* development of Co$_3$O$_4$ active catalysts for hydrogen evolution studies.

Results

Synthesis and spectroscopic characterization

2-Methoxyaniline and *ortho*-vanillin were mixed at the molar ratio 1 : 1 in the ethanol medium to synthesize the ligand **HL**, following our reported synthetic method.[35] The characterization data for **HL** is published by our group elsewhere.[35] The **Co^{mono}** complex was synthesized by the reaction of **HL** with cobalt(II) perchlorate hexahydrate, followed by NH$_4$NCS in 2 : 1 : 2 methanol (Scheme 1). The dicobalt(II) complex (**Co^{di}**) was prepared by a 2 : 1 reaction mixture of **HL** with hydrated cobalt(II) perchlorate in MeOH under slight warming conditions (40 °C) (Scheme 1). Nonetheless, both complexes can be synthesized with other cobalt salts like hydrated cobalt(II) nitrate and hydrated cobalt(II) chloride.
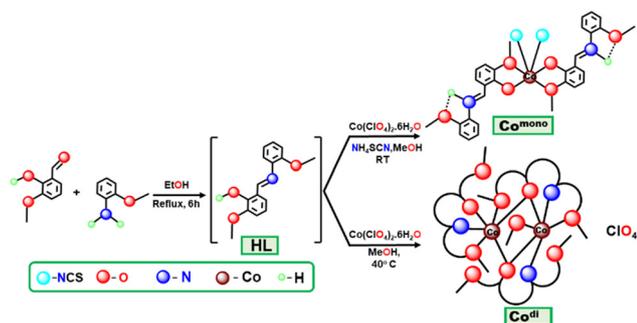
Scheme 1 Synthetic route of the cobalt(II) complexes.

The FT IR spectra for both the cobalt complexes are shown in Fig. S1 (detailed discussion in ESI†). The UV-Vis spectrum of **Co^mono** in the acetonitrile at room temperature displays the electronic bands at 270, 333, 434 and 636 nm (Fig. S2†). The bands at ~270 and 333 nm are assignable to the ligand-centric π–π*/n–π* transitions, while the optical band at 434 nm corresponds to the intra-ligand charge transition.[35] Further, a broad d–d band from 600 to 700 nm is noticed in the UV-Vis spectrum of **Co^mono**.[36] The electronic spectrum of **Co^di** in acetonitrile shows the appearance of the electronic bands at 292, 331 and 409 nm, addressing the π–π*/n–π* electronic transition of ligand origin and the phenoxo to Co(II) charge transition octahedral **Co^di** complex.[37]

Crystal structure description and morphological assessment

The X-ray crystal structure analyses of **Co^mono** and **Co^di** reveal that both the complexes crystallize in a monoclinic system with $I2/a$ and $P2_1/n$ space groups, respectively. However, the two complexes differ significantly in the ligational motifs of ligand to the formation of the coordination sphere of the Co(II) ions. However, the Co(II) centres in both complexes adopt an octahedral coordination geometry. The structural refinement parameter, bond distance, and bond angle tables of **Co^mono** and **Co^di** are given in Tables S1–S3.† In the view of the positions of the donor centres, **HL** is presumed to be a tetradentate (N,O)-type ligand; however, in the formation of **Co^mono**, the azomethine–N abstracts a proton from phenolic–OH lead to the zwitterionic form of **HL**. This phenomenon excludes the employment of all the donor sites with the Co(II) centre in **Co^mono**. Therefore, the protonated azomethine–N and the adjacent –OCH₃ in the ligand skeletal hampered its concurrent chelation property towards Co(II) ion. Thereby, the addition of two equivalents NCS⁻ into the reaction mixture of Co(II)–**HL** allows the coordination of NCS⁻ ions with the Co(II) ion and is accountable for developing the octahedral coordination geometry of **Co^mono** (Fig. 1a). The crystal structure of **Co^mono** indicates that a square plane is formed by the coordination of two phenoxo–O and one methoxy–O of **HL**, and thiocyanate–N coordination while the axial coordination is satisfied with the methoxy–O of **HL** and the second thiocyanate–N. The average Co(II)–O/N bond distance in the square plane is found to be 2.1022 Å, while the average axial bond distance Co(II)–O/N is
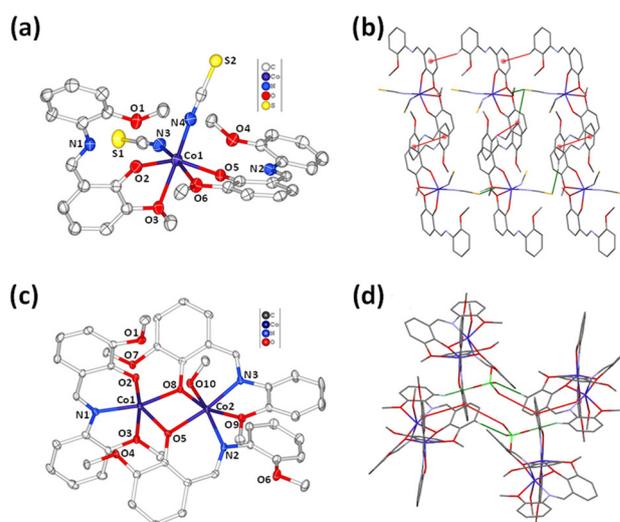

Fig. 1 (a) ORTEP plots of **Co^mono** at 30% probability; (b) π⋯π, C–H⋯π and S⋯H interactions mediated supramolecular framework of Comono in the crystalline state; (c) ORTEP plots of **Co^di** at 30% probability; ClO₄⁻ ion is omitted for clarity; (d) ClO₄⁻-mediated supramolecular architecture of **Co^di** in the solid state.

obtained as 2.1765 Å due to the axially elongated octahedron of **Co^mono**. The nature of supramolecular interactions in **Co^mono** has also been assessed by the extent of interaction in the development of a long-range crystalline framework. Notably, π⋯π, C–H⋯π and C–H⋯S interactions are actively operative in framing the supramolecular architecture (Fig. 1b). The non-covalent interaction parameter for **Co^mono** is summarized in Table S4.†

X-ray structure analysis of **Co^di** discloses that the asymmetric unit adopts three deprotonated **L⁻** units, two Co(II) centres, one coordinated methanol and perchlorate as a counter ion. In this structure, the ligational characteristics of the ligand are found to be interesting. The three ligand units show a different denticity as bi-, tri-, and tetradentate in coordination with the cobalt(II) centres. Probably, the phenolate-O-induced bridging between the Co(II) centres enables the metal ions under a crowding environment and imposes a steric hindrance among the donor sites. This results in the distal movement of the donor centres from the zone of coordination of the Co(II) centres (Fig. 1c). It is also evident that a linear geometric CH₃OH is seen to coordinate with one of the Co(II) centres due to the availability of a narrow channel. A perchlorate ion is also evident for balancing the residual cationic charge for the dinuclear cobalt(II) complex. The bidentate and tetradentate ligand units use their phenoxo-units to couple the Co(II) centres and form a doubly-phenoxo-coupled Co(II) dimer. The Co(II) ions in the bridging core form a distorted planar Co**1**–(μ-O5)(μ-O8)₂–Co**2** core with an angle of 22.56° between the Co**1**–O5–Co**2** plane and Co**1**–O8–Co**2** plane. In the Co**2** centre, O9, O8, O10, and N2 surround to compose an equatorial plane and O5 and N3 occupy the axial position. In the equatorial plane, the bond angle values for O9–Co2–N2

and O9–Co2–O10 are found to be 82.77 and 81.97°, while the angles O10–Co2–O8 and O8–Co2–N2 are noted as 92.41 and 106.88°, respectively. All the equatorial angles deviate greatly from the right angle. In contrast, the equatorial plane in Co1 comprises O5, O2, O7 and O3 atoms while O8 and N1 make the axial coordination. The equatorial bond angles, O5–Co1–O2, O5–Co1–O3, O2–Co1–O7, and O7–Co1–O3, are found to be 94.53, 87.52, 87.72 and 95.53, denoting a close occupancy to the right angles. The Co(II) complex is formed by the double μ-phenoxo bridges with a Co1···Co2 distance of 3.129(0) Å. In this **Co**^{di} complex, the role of perchlorate ion is revealed through the investigation of supramolecular interactions. It is revealed that the perchlorate–oxygen assembles three dinuclear units through intermolecular C–H···O interactions, which is further supported by π···π interactions to develop supramolecular crystalline architecture (Fig. 1d). The non-covalent interaction parameter for **Co**^{di} is given in Table S5.†

The morphology of the synthetic complexes has been judged with powder X-ray diffraction (PXRD), field emission scanning electron microscopy (FESEM), and electron dispersive X-ray (EDX) studies. The PXRD plots of **Co**^{mono} and **Co**^{di} (Fig. 2a and b) display intensified sharp characteristic peaks up to 2θ values of 50°, which is attributed to a noticeable crystallinity in the compounds. Additionally, the experimental and theoretical fitting of the PXRD pattern matches closely with each other in both the cobalt complexes, recommending their bulk purity in the crystalline phases. The FESEM images of complexes (Fig. 2c and d) suggest that **Co**^{mono} and **Co**^{di} exist in irregular-shaped flake-type particles. The average individual grain size of **Co**^{mono} and **Co**^{di} is estimated at ~0.415 μm and 0.759 μm, respectively. EDX analysis of the compounds (Fig. S3 and S4†) ensures a similar kind of elemental distribution, as evidenced by the elemental analysis and X-ray crystallography. Additionally, X-ray photoelectron spectroscopy (XPS) was carried out, which confirmed the presence of Co, C, N, S, and

O elements in **Co**^{mono} and Co, C, N, and O in **Co**^{di}. The XPS plot of both complexes is shown in the ESI (Fig. S5 and S6†).[38]

Magnetic characterization

The molar magnetic susceptibility (χ_M) measurement was performed on the cobalt complexes **Co**^{mono} and **Co**^{di} in the temperature range of 4.8–300 K under a 1.0 kOe field. The plots of $\chi_M T$ versus T and χ_M versus T for **Co**^{mono} and **Co**^{di} are shown in Fig. 3a and b. The observed room temperature $\chi_M T$ value for **Co**^{mono} (2.66 cm^3 mol^{-1}) is significantly larger than the theoretical value for an $S = 3/2$ case (i.e., 1.875 cm^3 mol^{-1} K; with $g = 2$) as it is expected for an unquenched Co(II) momentum. Upon cooling, $\chi_M T$ almost linearly decreases down to about 70 K. Below this temperature, $\chi_M T$ decreases more rapidly and reaches a $\chi_M T$ value of 1.58 cm^3 mol^{-1} at 4.8 K (Fig. 3a). The rapid decrease in the $\chi_M T$ value at low temperatures implies the presence of a high axial anisotropy of the crystal field, which is acting on the Co(II) moments. The Co–N/O bond distances (Fig. 3a1) and bond angles (Fig. 3a2) are in good agreement with the high spin conformation and in good correlation with the observed magnetic susceptibility value of the mononuclear **Co**^{mono} complex.[39]

On the contrary, the room temperature $\chi_M T$ value for **Co**^{di} was found to be 5.63 cm^3 mol^{-1} K, which is greater than that of an isolated octahedral Co(II) ion (3.75 cm^3 mol^{-1} K with $g = 2.0$ and $S = 3/2$) but lower than the expected magnetic value for
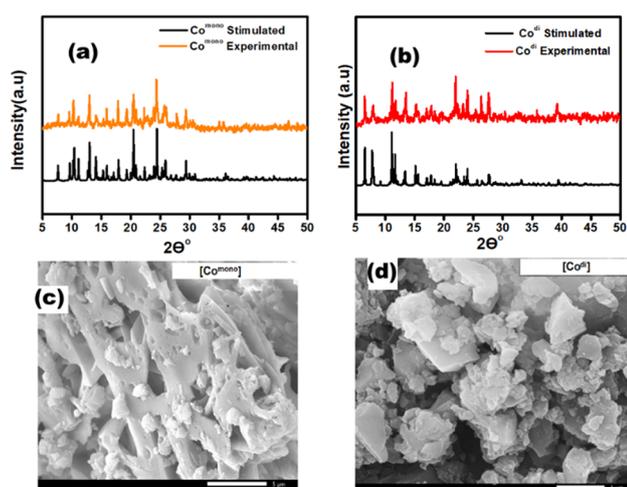

Fig. 2 (a) PXRD plots of **Co**^{mono}; (b) PXRD plots of **Co**^{di}; (c) scanning electron micrograph of **Co**^{mono}; (d) SEM image of **Co**^{di}.
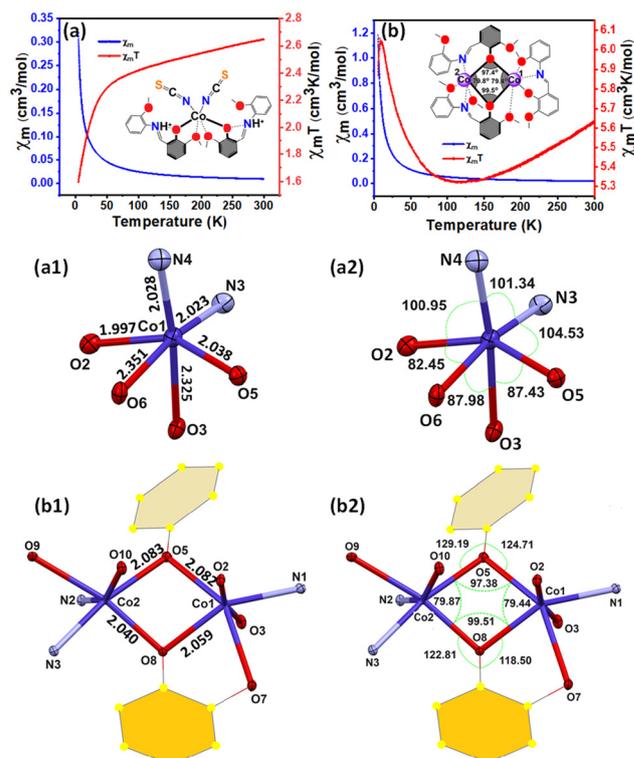

Fig. 3 Temperature variation of the $\chi_M T$ product as well as χ_M per **Co**^{mono} (a) and [Co$_2$O$_2$] cluster in **Co**^{di} (b); bottom: presentation of bond distances and bond angles in **Co**^{mono} (a1 and a2) and in **Co**^{di} (b1 and b2).

two octahedral Co(II) centres (Fig. 3b). This observation accounts for the presence of strong spin–orbit coupling between two Co(II) centres. Upon cooling, the $\chi_M T$ value primarily decreases to a value of 5.33 cm³ mol⁻¹ K till 150 K. Further lowering the temperature to 112 K, the $\chi_M T$ slowly decreases to reach a minimum of 5.31 cm³ mol⁻¹ from where the $\chi_M T$ value starts to increase again slowly up to 75 K. The dicobalt(II) complex maintains nearly a flat region from 150 to 75 K. Upon lowering the temperature, the $\chi_M T$ value starts to increase sharply till 8 K, showing a $\chi_M T$ value of 6.05 cm³ mol⁻¹. Further, the decrease in the temperature showed a drastic fall in the $\chi_M T$ value at 4.8 K.

To understand the dominance of magnetic interactions, the literature survey on the magnetic properties of the structural analogues diphenoxo-bridged dinuclear Co(II) complexes was carried out. The temperature-dependent magnetic characteristics from 300 to 8 K for the **Co^di** complex are attributed to the origin of the spin–orbit coupling effects and ferromagnetic interaction between two cobalt centres. The final fall of the magnetic values at 4.8 K could be ascribed to the partial depopulation of excited magnetic states, zero-field splitting effects, and/or intermolecular interactions.[40]

It is well-observed that μ-phenoxo-bridged dinuclear Co(II) complexes in most cases are dominated by antiferromagnetic (AF) interactions as AF contributions ($J_{z^2\_xy}$, $J_{z^2\_z^2}$, $J_{z^2\_x'^2-y'^2}$, $J_{x^2-y^2\_x'y'}$, $J_{x^2-y^2\_z'^2}$, $J_{x^2-y^2\_x'^2-y'^2}$), overcome the weaker ferromagnetic (F) contributions ($J_{xy\_x'y'}$, $J_{xy\_z'^2}$, $J_{xy\_x'^2-y'^2}$) in the Co₂O₂ system. Notably, four significant AF contributions are evident as $J_{x^2-y^2\_x'^2-y'^2}$ AF and $J_{z^2\_x'^2-y'^2}$ AF, followed by $J_{x^2-y^2\_z'^2}$ AF and $J_{z^2\_z'^2}$ AF, which coherently depend on the Co–O–Co angles. It is also observed that with the decrease in the Co–O–Co angle and closeness to the right angles, the AF contributions ($J_{x^2-y^2\_x'^2-y'^2}$ AF, $J_{z^2\_x'^2-y'^2}$ AF, $J_{x^2-y^2\_z'^2}$ AF and $J_{z^2\_z'^2}$ AF) decrease effectively without affecting the principal F contributions ($J_{xy\_x'^2-y'^2}$ F and $J_{xy\_z'^2}$ F) in Co–O–Co.[41] In the **Co^di** complex, the Co–O–Co angles (97.38 and 99.51°) in the synthetic dicobalt(II) complex (Fig. 3b2) are the prime contributory factor for the exhibition of weak ferromagnetic interaction (Scheme 2). In addition, the magnetic coupling between the two nuclei is significantly influenced by the dihedral angle (δ) between the M–O–M plane and the phenyl plane besides the M–O–M angles (γ) (Scheme 2).[42]
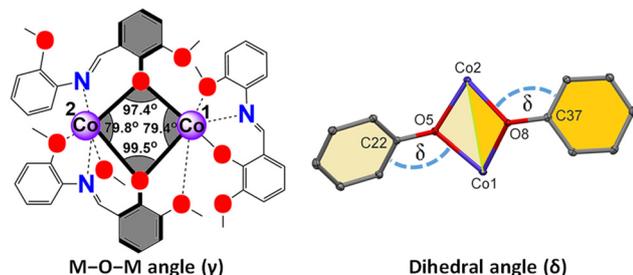
Scheme 2 Schematic presentation of M₂O₂ core with the M–O–M angle (γ) and dihedral angle (δ).

It is documented that a large dihedral angle may reduce the extent of AF interactions. Song *et al.* evaluated the correlation of the Co–O–Co angle and dihedral angle in a synthesized double-phenoxo-dicobalt(II) complex.[43] The researchers justified the relationship between the smaller Co–O–Co angle ($\gamma < 99.7°$) and the larger dihedral angle between the Co–O–Co plane and the phenyl plane ($\delta > 35.3°$), with the development of preferential ferromagnetic properties in the bis(phenoxo)-bridged Co₂O₂ system. In the synthetic **Co^di** complex, the Co(μ-O)₂–Co core adopts the angles (γ) of 97.38(5) and 99.51(5)° for Co1–O5–Co2 and Co1–O8–Co2, respectively, while the dihedral angles (δ) between the Co1–O5–Co2 and Co1–O8–Co2 plane and the phenyl plane are 41.320(64)° and 36.383(67)°, respectively (Scheme 2). Therefore, the effect of the Co–O–Co angle and dihedral angle in the **Co^di** complex ensures the switching of the magnetic coupling from antiferromagnetic to ferromagnetic properties. The Co–N/O bond distances (Fig. 3b1) are in good accordance with the reported bond distance values for doubly-phenoxo-bridged dicobalt(II) complex.[43] A table of comparison is additionally drawn to correlate the dihedral angle (δ) and M–O–M angles (γ) of the synthetic cobalt complexes with that of the reported complexes (Table S6†), recommending the weak ferromagnetic properties in the synthetic **Co^di** system.

Electrical transport property

The nature of the electrical conductivity of **Co^di** and **Co^mono** was assessed by examining the current–voltage (I–V) characteristics of the two fabricated Schottky devices, Al/**Co^di**/ITO (**device-A**) and Al/**Co^mono**/ITO (**device-B**). The I–V characteristics of the two fabricated devices were performed at the bias voltage ranging ± 5 V at room temperature (Fig. S7†). The conductivity of **device-A** was evaluated to be 6.89×10^{-4} S m⁻¹, which was ~17 times higher than that of **device-B** (3.90×10^{-5} S m⁻¹). The log I vs. V plot also supported the superior electrical conductance of **device-A** over **device-B**, as shown in Fig. S7† inset. The traditional I–V plot deviates from linearity, illustrating the pervasive non-ohmic conduction and consolidating the rectifying nature of the Schottky diode.

To reveal the role of temperature in the electric conductivity for both devices, the I–V characteristics were monitored for the fabricated devices at various temperatures (Fig. 4a and b). The results show that the electrical conductivity of both devices increases with the increase in temperature, highlighting the typical characteristic of a semiconducting material. The conductivity at different temperature values is given in Table S7.† Further, the diode parameters for **device-A** and **device-B** of charge transport properties like series resistance (R_S), ideality factor (η), and barrier height (ϕ_B) were evaluated by adopting the thermionic emission (TE) theory and Cheung's model following the eqn (S1)–(S7),† showing that the (R_S) and ideality factor (η) for the two devices were determined from the slope and intercept of the dV/d ln(I) vs. I plot (Fig. S8 and S9†). The barrier height for the two devices was extracted from the y-axis intercept of the $H(I)$ vs. I curve (Fig. S8 and S9†). The values of the ideality factor, barrier height and R_s are tabulated in
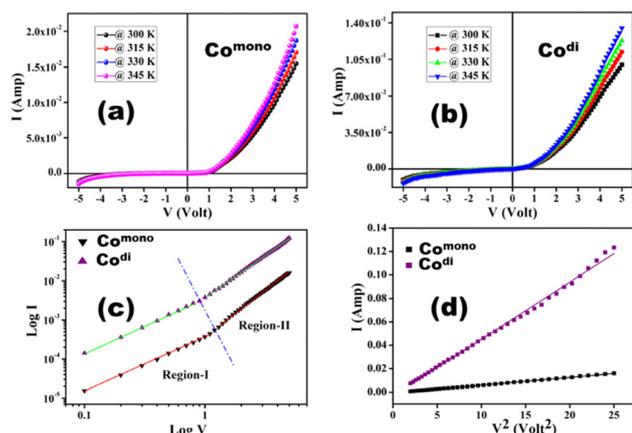
Fig. 4 (a) and (b) Temperature-dependent current–voltage (I–V) characteristic curve for the ITO/CO^{di}/Al and ITO/CO^{mono}/Al structured thin film devices; (c) logarithmic plot of I–V characteristics curve for **device-A** and **device-B**; (d) I vs. V^2 plot of the SCLC region.

Table S8.† It was observed that the values of the ideality factor (η) deviate from unity for both the devices. However, the extent of deviation was less in **device-A** than in **device-B**, which is attributed to a higher magnitude of inhomogeneities in the barrier height of **device-B**. Typically, electron and hole recombination rate has a high probability in the depletion region and there may be an existence of interface states and series resistance to account for the deviation of the ideality factor from unity.[44,45] Further, the I–V characteristic of the devices was explored in more detail by extracting the curves in the log scale to improve our understanding of charge transport mechanisms in the junction. In general, the current conduction mechanism is governed by the power law ($I \propto V^n$), where n is the slope of the I vs. V curve.[46] Here, the plot (Fig. 4c) exhibits two different regions under forward bias. At low bias voltage (**Region-I**), both the devices exhibit ohmic behaviour, i.e., ($I \propto V$) while the other region (**Region II**), which exhibits a variation of current with the square of bias voltage ($I \propto V^2$), displays typical characteristics of electrical conductance (Fig. 4d). In this region, the injected carriers exhibit more numbers than the background carriers, creating a space charge field that follows the space charge limited current (SCLC) mechanism.[47–49] Consequently, the Mott–Gurney (SCLC) eqn (S8)–(S10)† was employed to understand the device performance, which depends on the mobility (μ) and transit time (τ) of the devices. The mobility of **device-A** and **device-B** was found to be 9.21×10^{-5} m^2 V^{-1} s^{-1} and 2.02×10^{-5} m^2 V^{-1} s^{-1}, respectively, as calculated from the I versus V^2 plot. Additionally, the transit time of **device-A** and **device-B** was determined to be 1.70×10^{-9} s and 7.77×10^{-9} s, respectively, indicating higher electrons trapping probability of **device-B**. Moreover, the dielectric constant (ε_r) for **device-A** (0.7513) and **device-B** (0.4652) from the capacitance (C) vs. frequency (f) plot was estimated by eqn (S9)† (Fig. S10 and S11†). The value of the dielectric constant (ε_r) indicates the faster electrical transport in **device-A**. The charge transport parameters, viz.,

electrical mobility (μ), transit time (τ) and dielectric constant (ε_r), for both the devices are tabulated in Table S9.†

The impedance spectral analysis of Co^{mono} and Co^{di} was performed at room temperature. The Nyquist plot (Fig. S12†) represents the graphical plot of the imaginary part (Z'') vs. the real part (Z') of the obtained impedance. The Co^{di}, with a smaller semicircle area, exhibits a lower resistance of 5920 Ω than Co^{mono}, with a larger semicircle area corresponding to 12 700 Ω resistance. This signifies the low resistance and better electron transport activities in Co^{di}.[50]

Electrocatalytic hydrogen evolution reaction (HER)

The electrochemical properties of the synthetic cobalt complexes Co^{mono} and Co^{di} were initially measured with the cyclic voltammograms in ACN under an N$_2$ atmosphere with 0.1 M [(n-Bu)$_4$N]ClO$_4$ as the supporting electrolyte. In cyclic voltammetry, a three-electrode setup consisting of glassy carbon as the working electrode, platinum (Pt) as a counter electrode and Ag wire as a reference electrode was used. Co^{mono} shows a reduction wave at −0.85 V in the potential window from 0 to −1.2 (V vs. Ag wire), which correlates with the presence of the Co$^{II/I}$ species (Fig. S13†). The Co^{di} complex also shows a reduction wave at −1.03 (V vs. Ag wire) corresponding to the Co$^{II/I}$ redox couple (Fig. S13†). Previously reported values for the structurally analogous cobalt complexes confirm the metal–centric reduction from Co(ii) to Co(i).[15,18] To assess the redox nature of the synthetic ligand, **HL**, a cyclic voltammogram was recorded under a similar electrochemical condition, which did not impart any characteristic redox signal (Fig. S14†), suggesting its redox-inactive feature at that potential region in the electrochemical conditions.

The electrocatalytic fate of Co^{mono} and Co^{di} was examined in an electrocatalytic heterogeneous hydrogen evolution reaction (HER) in 0.1 M KOH solution. For this, a homogeneous ink was prepared by sonicating the electrocatalysts with Nafion and ethanol. The details of the preparation of homogeneous ink are described in ESI.† The homogeneous ink was drop-cast on the surface of GCE to examine the heterogeneous electrocatalysis in 0.1 M KOH. To validate the molecular inertness of Co^{mono} and Co^{di} catalysts during electrode ink preparation, we analysed the PXRD of the electrocatalyst after sonication. The PXRD pattern of the pure catalysts displayed a close match with the PXRD patterns of the recovered electrocatalysts after sonication (Fig. S15 and S16†), signifying that the molecular integrity of the catalysts was intact during the preparation of the electrode ink.

Additionally, to check the stability of the molecular complexes in 0.1 M KOH solution, both complexes were kept in the alkaline solution for 24 h. After 24 h, the electrocatalysts were recovered, recrystallized in methanol and then the PXRD were recorded (Fig. S15 and S16†). PXRD analysis suggests a close resemblance of the PXRD pattern between the pure and recovered catalysts. The PXRD comparison ensured the retention of the molecular integrity of the complexes in 0.1 M KOH after 24 h.[51]

After determining the molecular inertness of the complexes during the electrode's ink preparation and in 0.1 M KOH, both the electrocatalysts were immobilized on the surface of the working electrode with a similar mass loading of 0.212 mg cm^{-2}. In cyclic voltammetry, a three-electrode setup consisting of glassy carbon as the working electrode, platinum (Pt) as the counter electrode, and Ag/AgCl as the reference electrode (saturated with KCl) was used. The linear sweep voltammetry (LSV) in the cathodic direction was recorded for both complexes in 0.1 M KOH solution with a scan rate (v) of 5 mV s^{-1}. The overpotential (η) values were estimated as 574 mV and 525 mV for **Co^{mono}** and **Co^{di}**, respectively, at a current density of 10 mA cm^{-2} (Fig. 5a). The overpotential values for **Co^{mono}** and **Co^{di}** were found to be comparable with those of previously reported cobalt complexes with remarkable hydrogen evolution studies.[52–54]

For a deep understanding of the electrochemical nature of the cobalt complexes, the Tafel slope was derived from the Tafel plot profiling η against $\log j$ by following $\eta = b \log j + a$, where b and j represent the Tafel slope and current density, respectively (Fig. 5a inset). Many pioneers in this field expounded the mechanistic aspects of the alkaline HER through the Tafel slope.[55] The Tafel slope values for **Co^{mono}** and **Co^{di}** were evaluated at 115 and 146 mV dec^{-1}, respectively, demonstrating the Volmer–Heyrovsky step as the rate-determining step in electrocatalytic hydrogen evolution (Fig. 5a inset). To reveal the kinetic nature of the electrocatalytic hydrogen evolution studies, the onset potentials were derived as 0.456 and 0.376 V $vs.$ RHE for the **Co^{mono}** and **Co^{di}** electrocatalysts, respectively.

The estimation of active sites in the electroactive film was pursued with directly related surface area parameters, namely, electrochemical double-layer capacitance (C_{dl}), electrochemical active surface area (ECSA), and roughness factor (R_f). The C_{dl} of Co(II) electrocatalysts was determined from the CVs at the non-faradaic region recorded at different scan rates (Fig. 5b and Fig. S17†). The current values at the middle potential of the non-faradaic region were plotted against the scan rate and the linear slope, equivalent to the C_{dl} (Fig. S18† and Fig. 5c).[56–58] The C_{dl} value for **Co^{di}** (3.46 μF) is higher than **Co^{mono}** (2.50 μF), manifesting a higher electrical energy storage capacity for the **Co^{di}** catalyst. Subsequently, ECSA was also derived from eqn (S11).† The ECSA of **Co^{mono}** and **Co^{di}** were estimated at 0.091 cm^2 and 0.126 cm^2, respectively, validating the higher electrochemical activity for complex **Co^{di}** over **Co^{mono}**. Similarly, R_f was determined as 1.29 and 1.78 for **Co^{mono}** and **Co^{di}**, respectively, by eqn (S12).†[58]

The intrinsic activity of the cobalt complexes was determined by calculating the charge (Q), the number of active sites (n), and turnover frequency (TOF) using eqn (S13)–(S15).† The number of active sites (n) for **Co^{mono}** and **Co^{di}** was evaluated as 5.5610×10^{-8}, and 1.0296×10^{-8} mol, while TOFs were calculated as 0.0931 s^{-1} and 0.5033 s^{-1}, respectively. The electrochemical parameters, $viz.$, overpotential (η), Tafel slope (b), TOF, C_{dl}, ECSA, and R_f of the **Co^{mono}** and **Co^{di}** electrocatalyst, are tabulated in Table S10.†

The long-term electrochemical stability and durability of the synthetic cobalt(II) catalysts for hydrogen production in an alkaline water splitting were studied with constant potential electrolysis (CPE). The CPE was allowed to run for 6000 s at a constant potential at −0.49 V $vs.$ RHE for both **Co^{mono}** and **Co^{di}** in 0.1 M KOH. The CPE plots are displayed in Fig. S19.† The CPE plot for **Co^{di}** conveys the rapid synchronization of bubble accumulation and release throughout electrocatalysis whereas the current-time plot of **Co^{mono}** maintains a relatively slower release and accumulation of the bubble. However, the current density for the **Co^{di}** catalyst during CPE is higher than the current density for the **Co^{mono}** catalyst. Furthermore, the LSV of both cobalt electrocatalysts was recorded before and after CPE. For **Co^{mono}**, the LSV after CPE displayed an overpotential of 426 mV while for **Co^{di}**, it was found to be 412 mV. After CPE, we noticed lower η values for both cobalt electrocatalysts compared to the η values of the cobalt catalysts prior to CPE (Fig. S20 and S21†). The reduction in the η values for both the electrocatalysts is attributed to the more electrocatalytically active species, manifesting the in $situ$ generation of structurally transformed active species.[19] However, the overpotential of **Co^{di}** after CPE was lower with respect to **Co^{mono}**, signifying the transformation of more active species. The electrochemical parameter differences of both the catalysts before and after CPE are tabulated in Table S11.†

Furthermore, to gain more insight, CPEs for both catalysts were performed at a lower constant potential of −0.37 V $vs.$ RHE with an extended time of 5 h. The CPE plot of **Co^{mono}** displayed a subsequent rise in the current density from −2.18 mA cm^{-2} to −7.12 mA cm^{-2} during 5 h (Fig. S22†), while for **Co^{di}**, the current density increased from −2.33 mA cm^{-2} to −11.2 mA cm^{-2} (Fig. 5d). The gradual change in the current
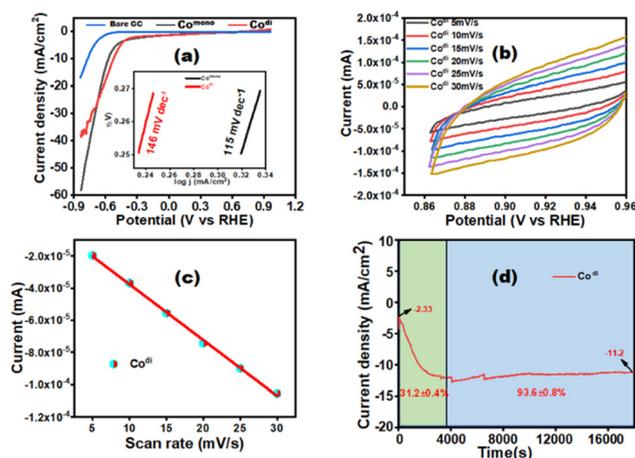

Fig. 5 (a) LSV of **Co^{mono}** (black), **Co^{di}** (red), and bare glassy carbon electrode (GCE, blue); inset: Tafel plot; (b) plot of current $vs.$ potential at different scan rates for the determination of double layer capacitance at the non-faradaic region for **Co^{di}**; (c) profile of the current $vs.$ scan rate variation for the calculation of electrochemical double-layer capacitance of **Co^{di}**; (d) CPE of **Co^{di}** performed at −0.37 (V $vs.$ RHE) in N$_2$-saturated water using 0.1 M KOH as the supporting electrolyte to determine the corresponding faradaic efficiency for hydrogen production.

density during CPE suggests that parallel faradaic processes are occurring during the electrocatalytic hydrogen evolution. The faradaic Efficiency (FE) calculation for the first 1 h of CPE was found to be 35.7% and 31.2% for **Co^{mono}** and **Co^{di}**, respectively, signifying some concurrent electrochemical processes during CPE. However, after one hour of CPE, **Co^{mono}** and **Co^{di}** displayed a steady current density with better FE of 89.8% and 93.6%, respectively. This confirms that the electrocatalysts experience significant dynamic irreversible activation within the first hour of CPE. In addition, multi-cycle CV (500 times) was performed for both complexes at 1000 mV s^{-1} scan rate in sweeping between 0.96 and −0.84 (V *vs.* RHE) (Fig. S23 and S24†). A significant current elevation was evident for both the catalysts. The multi-cycle CV analysis also consolidates the formation of more active catalytic species under the electrochemical conditions. However, the elevation in the current change is higher in magnitude for **Co^{di}** than that for **Co^{mono}**.

Upon confirming the concurrent generation of structurally derived active species, XPS analysis was conducted to investigate the nature of the recovered active species after HER. The high-resolution Co 2p XPS spectra for post-electrochemical species are shown in Fig. S25.† XPS analysis reveal a significant difference in the binding energy value of the pure complex and post-electrochemical species corresponding to Co 2p$_{3/2}$.[38,59] For **Co^{mono}**, the peak at 781.08 eV was shifted to 780.5 eV after HER. Similarly, the peak at 781.3 eV of **Co^{di}** shifted to 780.7 after HER (Fig. S25a and S25b†). Furthermore, the nature of post-electrochemical active species was elucidated by PXRD for **Co^{mono}** and **Co^{di}**. Post-CPE **Co^{mono}** and post-CPE **Co^{di}** species displayed a high similarity in the PXRD patterns (Fig. S26†). In both the cases, the characteristic peaks at 31.3, 36.9, 38.6, 44.9, 55.7 and 59.5 were evident, corresponding to the Co_3O_4 (JCPDS: 00-042-1467) (Fig. S26†). The SEM images of the post-CPE cobalt species were also recorded to reveal the changes in the morphology between the cobalt complexes and the post-CPE cobalt species (Fig. S27†). The distinct change in the morphology and the particle size suggests the *in situ* transformations of the molecular complexes into cobalt oxide electrocatalysts.

This observation reveals that **Co^{mono}** and **Co^{di}** pre-catalysts under electrochemical conditions undergo irreversible activation, leading to Co_3O_4 active catalysts. The lability associated with the cobalt complexes may be accounted for in light of the X-ray structures of the complexes. It is observed that the utilization of lower denticity (two-donors) by the synthetic polydentate (four-donors) chelating ligand in the formation of the **Co^{mono}** complex imposes relatively higher lability to the complex, which is attributed to the prompt hydrolysis tendency of **Co^{mono}** under electrochemical conditions. In contrast, the chelating ligand behaves as a multidentate ligand (4/3/2-donor) in the formation of the dinuclear cobalt complex, where the chelating-cum-bridging coordination modes by the ligand transport into its active species in the electrochemical condition. However, **Co^{di}**-derived active Co_3O_4 species in the electrochemical conditions showed better activity compared to

the **Co^{mono}**-derived Co_3O_4 species owing to the differences in the particle size and morphology.

Nonetheless, the heterogeneous nature of both the catalysts was confirmed by the wash test.[60] In the wash test, the catalysts were initially subjected to CPE at a constant potential of −0.49 V *vs.* RHE for 6000 s. Afterwards, the working electrode was replaced by a fresh GC electrode in the same solution and CPE was taken under a similar electrochemical condition. The CPE of fresh GCE was found to be silent for both the cobalt catalysts (Fig. S28 and S29†). This observation confirmed that the solution did not contain any active electrocatalysts as well as no dissolution of Pt-electrode occurred in the electrocatalytic HER, which ensures the heterogeneous nature of the electrocatalysis.

Conclusion

In summary, two new cobalt(ɪɪ) complexes, **Co^{mono}** and **Co^{di}**, have been synthesized and structurally characterized. The crystal structure analysis reveals a unique structural feature for **Co^{mono}**, exhibiting a two-donor sites coordination from the tetradentate ligand backbone, conferring a zwitter ionic stabilization to the synthetic ligand in **Co^{mono}**, while the dicobalt(ɪɪ) complex (**Co^{di}**) adopts diphenoxo-bridged cobalt(ɪɪ) centres incorporating bidentate, tridentate and tetradentate modes of the three ligand units, creating an octahedral coordination environment for both the Co(ɪɪ) centres. Temperature-dependent magnetic susceptibility measurements of **Co^{mono}** direct the typical paramagnetic characteristics of the complex. On the contrary, the effect of the Co–O–Co angle and dihedral angle is evident in the **Co^{di}** complex, attributed to the switching of the antiferromagnetic to the ferromagnetic properties at low temperatures. Further, **Co^{di}** exhibited better electron transport properties, as evidenced by its lower transit time, 1.70×10^{-9} s, relative to the transit time, 7.77×10^{-9} s in **Co^{mono}**. The impedance spectral analysis reveals a lower electrical transport resistance, 5920 Ω, for **Co^{di}** compared to the resistance (12 700 Ω) for **Co^{mono}**. The electrochemical studies estimate the overpotential of 574 and 525 mV for **Co^{mono}** and **Co^{di}** to achieve 10 mA cm^{-2} with corresponding Tafel slopes 115 and 146 mV, respectively. Additionally, **Co^{mono}** and **Co^{di}** show the onset potentials 0.456 and 0.376 V *vs.* RHE, respectively. However, long-term CPE analysis for **Co^{mono}** and **Co^{di}** in the alkaline HER revealed the irreversible structural transformations for both the electrocatalysts into more active catalysts, which typically formed within the first hour of CPE and recommended parallel faradaic processes for the first hour of electrocatalysis for both the cobalt catalysts. The multi-cycle CV analysis for **Co^{mono}** and **Co^{di}** in the KOH displayed a significant elevation in the current density with the progress of time and validated the pre-catalytic nature of the complexes. The significant reduction in the overpotential after CPE also confirmed the *in situ* structural transformation. XPS and PXRD analysis confirmed the development of Co_3O_4 active catalysts for both the cases. Overall, **Co^{di}**-derived Co_3O_4 active catalysts turned out to

be better electrocatalysts than Co^{mono}-derived Co_3O_4 active catalysts owing to their smaller particle size and corresponding morphology. The better electrical transport, ferromagnetic and electrochemical properties contribute to the superior electrocatalytic candidature of the Co^{di} complex over the Co^{mono} complex. The fine-tuning of the electronic and structural properties of the molecular complexes may significantly escalate the electrocatalytic efficiency of the hydrogen economy. The cobalt complexes also offer an important scope for magnetic HER, a limitedly explored area for hydrogen production.

Author contributions

Subhajit Saha: Conceptualization, formal analysis, methodology, investigation; Nilankar Diyali: Formal analysis, methodology, investigation; Sangharaj Diyali: Formal analysis, investigation; Subhra Jyoti Panda: Formal analysis, validation; Mainak Das: Formal analysis, investigation; Sobhna Acharya: Formal analysis, investigation; Prafullya Kumar Mudi: Formal analysis, methodology, investigation; Monika Singh: Formal analysis, methodology; Partha Pratim Ray: Formal analysis, investigation; Chandra Shekhar Purohit: Formal analysis, validation; Bhaskar Biswas: Conceptualization, writing-reviewing and editing, supervision.

Data availability

The data supporting this article have been included as part of the ESI.†

Conflicts of interest

There are no conflicts of interest to declare.

Acknowledgements

References

1 P. J. Megia, A. J. Vizcaino, J. A. Calles and A. Carrero, *Energy Fuels*, 2021, **35**, 16403–16415.

2 S. Ehsan and M. A. Wahid, *Renewable Sustainable Energy Rev.*, 2016, **57**, 850–866.

3 F. Dawood, M. Anda and G. M. Shafiullah, *Int. J. Hydrogen Energy*, 2020, **45**, 3847–3869.

4 A. Debnath, S. Diyali, M. Das, S. J. Panda, D. Mondal, D. Dhak, C. S. Purohit, P. P. Ray and B. Biswas, *Dalton Trans.*, 2023, **52**, 8850–8856.

5 Y. Shi and B. Zhang, *Chem. Soc. Rev.*, 2016, **45**, 1529–1541.

6 W. Li, H. Zhang, K. Zhang, Z. Cheng, H. Chen, G. Tan, X. Feng, L. Wang and S. Mu, *Chem. Commun.*, 2023, **59**, 4750–4753.

7 S. Diyali, N. Diyali and B. Biswas, *Coord. Chem. Rev.*, 2024, **500**, 215496.

8 C. H. Lee, D. K. Dogutan and D. G. Nocera, *J. Am. Chem. Soc.*, 2011, **133**, 8775–8777.

9 E. S. Wiedner, A. M. Appel, D. L. Dubois and R. M. Bullock, *Inorg. Chem.*, 2013, **52**, 14391–14403.

10 S. K. Mandal, C. Sunil and J. Choudhury, *ACS Catal.*, 2024, **14**, 2058–2070.

11 S. Khandelwal, A. Zamader, V. Nagayach, D. Dolui, A. Q. Mir and A. Dutta, *ACS Catal.*, 2019, **9**, 2334–2344.

12 N. Diyali, M. Chettri, S. Saha, A. Saha, S. Kundu, D. Mondal, D. Dhak and B. Biswas, *CrystEngComm*, 2023, **25**, 6837–6844.

13 J. E. Armstrong, P. M. Crossland, M. A. Frank, M. J. Van Dongen and W. R. McNamara, *Dalton Trans.*, 2016, **45**, 5430–5433.

14 R. Gueret, C. E. Castillo, M. Rebarz, F. Thomas, M. Sliwa, J. Chauvin, B. Dautreppe, J. Pécaut, J. Fortage and M. N. Collomb, *Inorg. Chem.*, 2019, **58**, 9043–9056.

15 S. Kundu, N. Diyali, S. Saha, M. Chettri, R. K. Mahato, S. K. Agrawalla, C. S. Purogit and B. Biswas, *Inorg. Chim. Acta*, 2024, **570**, 122161.

16 R. Sun, X. Huang, J. Jiang, W. Xu, S. Zhou, Y. Wei, M. Li, Y. Chena and S. Han, *Dalton Trans.*, 2022, **51**, 15205–15226.

17 G. Sarkar, N. Diyali, B. Mondal, S. K. Agrawalla, C. S. Purohit, H. S. Das and B. Biswas, *Appl. Organomet. Chem.*, 2024, e7544.

18 M. Raj, K. Makhal, A. Mishra, B. S. Mallik and S. K. Padhi, *Inorg. Chem.*, 2023, 10993–11008.

19 N. Kaeffer, A. Morozan, J. Fize, E. Martinez, L. Guetaz and V. Artero, *ACS Catal.*, 2016, **6**, 3727–3737.

20 J. Schild, B. Reuillard, A. Morozan, P. Chenevier, E. Gravel, E. Doris and V. Artero, *J. Am. Chem. Soc.*, 2021, **143**, 18150–18158.

21 V. A. Larson and N. Lehnert, *ACS Catal.*, 2024, **14**, 192–210.

22 W. Zheng, M. Liu and L. Y. S. Lee, *ACS Energy Lett.*, 2020, 3260–3264.

23 E. Benazzi, F. Begato, A. Niorettini, L. Destro, K. Wurst, G. Licini, S. Agnoli, C. Zonta and M. Natali, *J. Mater. Chem. A*, 2021, **9**, 20032–20039.

24 J. Kumar Yadav, B. Singh, S. K. Pal, N. Singh, P. Lama, A. Indra and K. Kumar, *Dalton Trans.*, 2022, **52**, 936–946.

25 C. Zhang, E. Prignot, O. Jeannin, A. Vacher, D. Dragoe, F. Camerel, Z. Halime and R. Gramage-Doria, *ACS Catal.*, 2023, **13**, 2367–2373.

26 C. S. Anensong Djadock, S. Vengatesan, A. C. Tagne Kuate, J. Ngoune, S. Ravichandran and S. Vasudevan, *Catal. Sci. Technol.*, 2023, **13**, 2184–2200.

27 A. Zamader, B. Reuillard, P. Marcasuzaa, A. Bousquet, L. Billon, J. J. Espí Gallart, G. Berggren and V. Artero, *ACS Catal.*, 2023, **13**, 1246–1256.

28 Y. Yin, Y. Zhang, T. Gao, T. Yao, X. Zhang, J. Han, X. Wang, Z. Zhang, P. Xu, P. Zhang, X. Cao, B. Song and S. Jin, *Adv. Mater.*, 2017, **29**, 1–8.

29 M. Zheng, Q. Chen and Q. Zhong, *Dalton Trans.*, 2021, **50**, 13320–13328.

30 B. Mao, P. Sun, Y. Jiang, T. Meng, D. Guo, J. Qin and M. Cao, *Angew. Chem., Int. Ed.*, 2020, **59**, 15232–15237.

31 K. L. Knoche Gupta, H. C. Lee and J. Leddy, *ACS Phys. Chem. Au*, 2024, **4**, 148–159.

32 K. S. R. Dadallagei, D. L. Parr IV, J. R. Coduto, A. Lazicki, S. DeBie, C. D. Haas and J. Leddy, *J. Electrochem. Soc.*, 2023, **170**, 086508.

33 W. Zhou, M. Chen, M. Guo, A. Hong, T. Yu, X. Luo, C. Yuan, W. Lei and S. Wang, *Nano Lett.*, 2020, **20**, 2923–2930.

34 X. Feng, Y. Q. Feng, J. J. Chen, S. W. Ng, L. Y. Wang and J. Z. Guo, *Dalton Trans.*, 2015, **44**, 804–816.

35 P. Kumar Mudi, N. Bandopadhyay, M. Joshi, M. Shit, S. Paul, A. Roy Choudhury and B. Biswas, *Inorg. Chim. Acta*, 2020, **505**, 119468.

36 M. Garai, D. Dey, H. R. Yadav, M. Maji, A. R. Choudhury and B. Biswas, *J. Chem. Sci.*, 2017, **129**, 1513–1520.

37 Y. H. Chen, S. J. Chen, J. Q. Li, Z. Wu, G. H. Lee, Y. H. Liu, W. T. Cheng, C. Y. Yeh and C. H. Peng, *J. Polym. Sci.*, 2020, **58**, 101–113.

38 A. Joshi, A. Gaur, P. Sood and M. Singh, *Inorg. Chem.*, 2021, **60**, 12685–12690.

39 R. Díaz-Torres, M. Menelaou, O. Roubeau, A. Sorrenti, G. Brandariz-De-Pedro, E. C. Sañudo, S. J. Teat, J. Fraxedas, E. Ruiz and N. Aliaga-Alcalde, *Chem. Sci.*, 2016, **7**, 2793–2803.

40 M. Fondo, J. Doejo, A. M. García-Deibe, J. Sanmartín-Matalobos, R. Vicente, M. S. El-Fallah, M. Amoza and E. Ruiz, *Inorg. Chem.*, 2016, **55**, 11707–11715.

41 R. Hotzelmann, K. Wieghardt, U. Flörke, H. Jürgen Haupt, D. C. Weatherburn, J. Bonvoisin, G. Blondin and J. J. Girerd, *J. Am. Chem. Soc.*, 1992, **114**, 1681–1696.

42 V. Archana, Y. Imamura, H. Sakiyama and M. Hada, *Bull. Chem. Soc. Jpn.*, 2016, **89**, 657–665.

43 X. J. Song and X. M. Xue, *ACS Omega*, 2020, **5**, 8347–8354.

44 M. Campos, L. O. S. Bulhões and C. A. Lindino, *Sens. Actuators, A*, 2000, **87**, 67–71.

45 R. K. Gupta and F. Yakuphanoglu, *Sol. Energy*, 2012, **86**, 1539–1545.

46 A. Dey, S. Middya, R. Jana, M. Das, J. Datta, A. Layek and P. P. Ray, *J. Mater. Sci.: Mater. Electron.*, 2016, **27**, 6325–6335.

47 R. Jana, A. Dey, M. Das, J. Datta, P. Das and P. P. Ray, *Appl. Surf. Sci.*, 2018, **452**, 155–164.

48 A. Jain, P. Kumar, S. C. Jain, V. Kumar, R. Kaur and R. M. Mehra, *J. Appl. Phys.*, 2007, **102**, 94505–94509.

49 M. Das, J. Datta, R. Jana, S. Sil, S. Halder and P. P. Ray, *New J. Chem.*, 2017, **41**, 5476–5486.

50 K. S. Das, B. Pal, S. Saha, S. Akhtar, A. De, P. P. Ray and R. Mondal, *Dalton Trans.*, 2020, **49**, 17005–17016.

51 E. M. Manohar, H. N. Dhandapani, S. Roy and R. Pełka, *Inorg. Chem.*, 2024, **63**, 4883–4897.

52 B. Kandemir, L. Kubie, Y. Guo, B. Sheldon and K. L. Bren, *Inorg. Chem.*, 2016, **55**, 1355–1357.

53 B. Mondal, K. Sengupta, A. Rana, A. Mahammed, M. Botoshansky, S. G. Dey, Z. Gross and A. Dey, *Inorg. Chem.*, 2013, **52**, 3381–3387.

54 G. Xu, H. Lei, G. Zhou, C. Zhang, L. Xie, W. Zhang and R. Cao, *Chem. Commun.*, 2019, **55**, 12647–12650.

55 K. Biradha, A. Goswami and R. Moi, *Chem. Commun.*, 2020, **56**, 10824–10842.

56 B. Mohanty, M. Ghorbani-Asl, S. Kretschmer, A. Ghosh, P. Guha, S. K. Panda, B. Jena, A. V. Krasheninnikov and B. K. Jena, *ACS Catal.*, 2018, **8**, 1683–1689.

57 Z. Zhou, L. Wei, Y. Wang, H. E. Karahan, Z. Chen, Y. Lei, X. Chen, S. Zhai, X. Liao and Y. Chen, *J. Mater. Chem. A*, 2017, **5**, 20390–20397.

58 A. Goswami, D. Ghosh and D. Pradhan, *ACS Appl. Mater. Interfaces*, 2022, **14**, 29722–29734.

59 M. C. Biesinger, B. P. Payne, A. P. Grosvenor, L. W. M. Lau, A. R. Gerson and R. S. C. Smart, *Appl. Surf. Sci.*, 2011, **257**, 2717–2730.

60 K. Chen, D. Ray, M. E. Ziebel, C. A. Gaggioli, L. Gagliardi and S. C. Marinescu, *ACS Appl. Mater. Interfaces*, 2021, **13**, 34419–34427.